All-solid-state artificial Z-scheme porous g-C$_3$N$_4$/Sn$_2$S$_3$-DETA heterostructure photocatalyst with enhanced performance in photocatalytic CO$_2$ reduction

Yao Huo[a,1], Jinfeng Zhang[a,1], Kai Dai[a,*], Qiang Li[a], Jiali Lv[b,c], Guangping Zhu[a], Changhao Liang[b,c,**]

[a] College of Physics and Electronic Information, Anhui Key Laboratory of Energetic Materials, Huaibei Normal University, Huaibei, 235000, PR China
[b] Key Laboratory of Materials Physics and Anhui Key Laboratory of Nanomaterials and Nanotechnology, Institute of Solid State Physics, Chinese Academy of Sciences, Hefei, 230021, PR China
[c] Hefei National Laboratory for Physical Sciences at the Microscale, University of Science and Technology of China, Hefei, 230026, PR China

ARTICLE INFO

ABSTRACT

Nowadays, the increasing CO$_2$ emissions have attracted widespread attentions and it is necessary to reduce CO$_2$ emissions to solve the global warming problem. So photocatalytic reduction of CO$_2$ into chemical fuels is a promising strategy. Here, a Z-scheme porous g-C$_3$N$_4$/Sn$_2$S$_3$-diethylenetriamine (Pg-C$_3$N$_4$/Sn$_2$S$_3$-DETA) composite without an electron intermediary is designed. Photocatalytic performance of the as-fabricated samples is investigated on the basis of photocatalytic CO$_2$ reduction (PCR) to form CH$_4$ and CH$_3$OH. We find that the Z-scheme heterostructure photocatalysts show a higher PCR performance than Pg-C$_3$N$_4$ and Sn$_2$S$_3$-DETA. An optimized Pg-C$_3$N$_4$/Sn$_2$S$_3$-DETA heterostructure sample displays high CH$_4$ production rate of 4.84 μmol h^{-1} g^{-1} and CH$_3$OH-production rate of 1.35 μmol h^{-1} g^{-1} with 5% Pg-C$_3$N$_4$ content. The superior PCR performance could be ascribed to the special structure of a direct Z-scheme Pg-C$_3$N$_4$/Sn$_2$S$_3$-DETA photocatalyst, which is beneficial to efficient separation of electron-hole pairs. Density functional theory (DFT) calculation further confirms the presence of direct Z-scheme mechanism. This Z-scheme heterostructure photocatalyst with superior performance may inaugurate the perspective on a new promising hierarchy of materials on CO$_2$ photoreduction.

1. Introduction

With the development of society and economy, energy and environment have drawn widespread attention [1]. Carbon dioxide (CO$_2$) is considered to be greenhouse gas which causes global warming. "Negative carbon economy" is regarded as a way to absorb carbon dioxide-based sustainable model and this phenomenon is gradually recognized by the society. Therefore, one of the best solution to this issue is to convert CO$_2$ to renewable fuels by utilizing solar energy [2–5]. Nowadays, plenty of semiconductors, such as TiO$_2$ [6,7], BiVO$_4$ [8,9] and Zn$_2$GeO$_4$ [10,11], and metal-organic frameworks (MOFs) have been reported for photocatalytic CO$_2$ reduction (PCR) to produce valuable chemicals [12–14]. However, the efficiency of single-phase semiconductor photocatalysts is quiet low due to the high recombination of electron-hole(e$^-$-h$^+$) pairs [15,16]. There are several strategies for enhancing the efficiency of PCR, including the deposition of metal oxides or noble metals onto photocatalysts [17–19], fabrication of nanomaterials with different morphologies or crystalline structures [20,21]. But the progresses applied in this field are unsatisfactory due to low efficiency [22,23]. Among the various semiconductors which have been tested, graphitic carbon nitride (g-C$_3$N$_4$) plays a significant role in solar-to-fuels conversion due to nonmetal, low cost, great photostablity, nontoxicity and appropriate band structure [24,25]. Bulk g-C$_3$N$_4$, usually synthesized by thermal polycondensated carbon-nitrogen containing organic precursors, its photocatalytic activity is unsatisfactory because of its poor specific surface area, undesirable visible light utilization and rapid recombination of e$^-$-h$^+$ pairs [26,27]. Therefore, photocatalytic activity of conventional g-C$_3$N$_4$

is not enough for practical application. To solve this problem, some efforts have been carried out in optimizing the structure and surface chemical state of g-C_3N_4 for improving the photocatalytic activity [28,29].

In nature, green plants can harvest sunlight efficiently to convert CO_2 and H_2O into carbohydrates and O_2. Inspired by this phenomenon, researchers intend to develop an artificial photosynthetic system by a conceptual mechanism in order to imitate natural photosynthesis. Researchers design an artificial Z-scheme photosynthetic system with a high efficiency by simulating a Z-scheme mechanism in the chloroplast [30,31]. As for Z-scheme photocalysts, such as Bi_2MoO_6/CdS-diethylenetriamine (DETA) [32], CdS/WO_3 [33], CdS/$BiVO_4$ [34], $CoTiO_3$/g-C_3N_4 [35], g-C_3N_4/Au/CdS [36] and black phosphorus/$BiVO_4$ [37], have been successfully prepared. These hybrid materials display vital advantages in the separation of photoexcited e^- and h^+. Besides, oxidation and reduction centers occur in different sites, which is beneficial to decrease the by-product in the photocatalytic reaction. The Z-scheme system use high conduction band minimum (CBM) of one conductor and a low valence band maximum (VBM) of another photocatalyst [38,39], which makes contributions to providing large overpotentials in photocatalytic reactions.

Porous g-C_3N_4 (Pg-C_3N_4) with narrow band gap of 2.62 eV has attracted much attention due to high stability and efficiency in the field of photocatalysis in recent years [40,41]. The conduction band (CB) edge at -1.17 eV offers Pg-C_3N_4 strong reduction power in photoexcitation. When the Pg-C_3N_4 nanosheets were dispersed in water, the abundant surface groups and negative charges make it become an ideal supporting material for coupling with other photocatalysts [42,43]. As for metal sulfides, they are usually considered a promising material for coupling with other semiconductors because of their narrow band gap [44,45]. For example, CdS has narrow band gap of $2.2 \sim 2.6$ eV and a suitable CB edge position, thus it has been used frequently in photocatalysis. However, the high toxicity of CdS has limited its practical usage [46,47]. Nowadays, Sn_2S_3 has attracted attention as important member of visible light driven photocalysis because of narrow band gap, lower price and environmentally friendly elemental components. However, PCR performance of Sn_2S_3-based photocatalyst has not been reported.

In this work, we prepared a high efficient hybrid photocatalyst composed of as-prepared organic-inorganic Sn_2S_3-DETA nanorod hybrids which grow on dispersed Pg-C_3N_4 nanosheets to form Z-scheme heterostructures. In this work, organic-inorganic Pg-C_3N_4/Sn_2S_3-DETA composite has superior photoreduction CO_2 performance, large surface area, controlled band structure, and high photostability, which is crucial to the introduction of DETA. Not only DETA improves the photocatalytic, optical and morphological properties [48], but they make Sn_2S_3-DETA well dispersed on the surface of Pg-C_3N_4 [49,50]. Furthermore, DETA molecule also plays a vital function in promoting PCR reaction [51]. Therefore, the structure of organic-inorganic Sn_2S_3-DETA hybrid makes great contributions to combining organic molecules and inorganic components [52,53]. The high visible-light absorption and suitable CB potential of the all-solid-state Z-scheme Pg-C_3N_4/Sn_2S_3-DETA are closely related to outstanding photoreduction CO_2 performance. Finally, the effects of Z-scheme photocatalyst Pg-C_3N_4/Sn_2S_3-DETA on the morphological characteristics, structure and photoreduction activity were explored and discussed in detail.

2. Experimental

2.1. Raw materials

Urea, sulfourea, tin chloride pentahydrate ($SnCl_4 \cdot 5H_2O$), absolute ethyl alcohol (EA), barium sulfate ($BaSO_4$), Sodium Bicarbonate ($NaHCO_3$), hydrochloric acid ($36\% \sim 38\%$ HCl), thioacetamide (TAA), DETA, polyethylene glycol (PEG 20,000), sulphuric acid ($95\% \sim 98\%$ H_2SO_4) and sodium sulfate ($NaSO_4$) were obtained by Shanghai

Chemical Reagent Corp. (P.R. China). NaH$^{13}CO_3$ were purchased by Cambridge Isotope Laboratories Inc. (USA).

2.2. Synthesis of Pg-C_3N_4

Yellow Pg-C_3N_4 powder was prepared by heating urea and sulfourea in accordance with the ratio of 3 to 1. Urea and sulfourea powder were heated to 823 K for 2 h. Then let the sample cool to room temperature, Pg-C_3N_4 was ultimately obtained in powder form.

2.3. Fabrication of Pg-C_3N_4/Sn_2S_3-DETA composite

Pg-C_3N_4/Sn_2S_3-DETA composite was prepared by a hydrothermal process. In the procedure, a certain of the Pg-C_3N_4 was dispersed in the solution premade by dissolving 1.402 g $SnCl_4 \cdot 5H_2O$ and 0.6 g TAA into the mixed solution of 15 mL DETA and 20 mL 18 MΩ deionized water (DW). The as-prepared mixture was dispersed by ultrasonic cell grinder. Then, the mixture was sealed at 50 mL autoclave and warmed at 453 K for 12 h. Eventually, Pg-C_3N_4/Sn_2S_3-DETA was obtained by washing with DW and drying at 313 K in lyophilization for 10 h. To investigate PCR performance of different Pg-C_3N_4/Sn_2S_3-DETA composites, the weight percentages of Pg-C_3N_4 varied by changing the weight ratio of Pg-C_3N_4, and the samples were labeled as 0%, 1%, 5%, 10% and 15% Pg-C_3N_4/Sn_2S_3-DETA.

2.4. Characterization

The chemical compositions of Pg-C_3N_4/Sn_2S_3-DETA were measured by Fourier transforms infrared spectroscopy (FT-IR Nicolet 6700) and X-ray photoelectron spectroscopy (XPS Thermo ESCALAB 250). The optical performance of Sn_2S_3-DETA, Pg-C_3N_4 and Pg-C_3N_4/Sn_2S_3-DETA was conducted by photoluminescence spectroscopy (PL FLS920) and UV–vis-NIR diffuse reflectance spectroscopy (PerkinElmer Lambda 950) measurements. The crystal structures of Sn_2S_3-DETA, Pg-C_3N_4 and Pg-C_3N_4/Sn_2S_3-DETA were recorded by X-ray diffraction (XRD Rigaku D/MAX 24000 diffractometer). The surface morphologies and elemental mapping images of the Pg-C_3N_4/Sn_2S_3-DETA were characterized using a transmission electron microscopy (HRTEM JEOL JEM-2010) equipped with an x-act energy dispersive spectrometer (EDS INCA) in high vacuum environment. The Brunauer-Emmett-Teller (BET) specific surface area value (S_{BET}) was estimated on a N_2 gas adsorption-desorption apparatus (ASAP 2040, Micrometrics Inc.). Methane labeled by ^{13}C and ^{12}C were recorded with gas chromatography-mass spectrometer (GC–MS Agilent Technologies 7890B GC system with 5977B MSD, USA). Photoelectrochemical measurement was investigated by common electrochemical system (Shanghai Chenhua CHI-660D) with a 1 cm^2 Pt sheet, a saturated calomel electrode (SCE) and 1 M Na_2SO_4 as the counter electrode, the reference electrode and the electrolyte, respectively. The working electrodes were fabricated as previous reported [54]. 100 mg photocatalyst mixed with 20 mg PEG and 0.5 mL DW were mixed and then injected onto ITO glass. Finally, the working electrodes dried and calcined at 523 K for 4 h to remove the PEG 20,000 and water.

2.5. Evaluation of PCR performance

The photocatalytic activities of as-obtained samples were investigated under visible light excitation ($\lambda > 420$ nm), as indicated in Fig. S1. Characteristically, 100 mg of sample was ultrasonically in 10 mL of DW and then the mixture was transferred to the 200 mL double-neck gyalectiform home-made flask with a groove at one neck. Then, the water was evaporated at 80 °C for 3 h and the photocatalyst was put as a flat film on the bottom of the flask. Subsequently, the flask was sealed with N_2 gas environment. Then, 0.5 mL of HCl (4 M) was injected into the groove to react with 0.12 g $NaHCO_3$ and a mixed gas of CO_2 and H_2O was obtained from this reaction process. Eventually, the
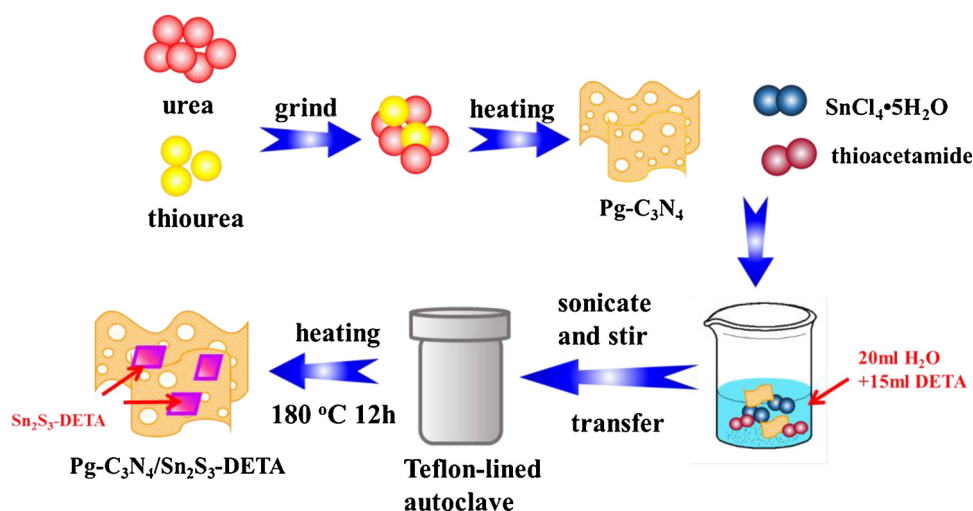
Fig. 1. Schematic illustration of the preparation process for Pg-C$_3$N$_4$/Sn$_2$S$_3$-DETA.

sealed flask reactor was irradiated by 300 W Xe lamp (CEL-HXF300, Beijing Aulight Inc.). The generated gas products was sampled by a headspace injector and analyzed by the gas chromatograph (GC-2014C, Shimadzu). The apparent quantum efficiency (QE) for PCR was tested and calculated according to Eq. (1) [55]:

$$QE\,[\%] = \frac{number\,of\,reacted\,electrons}{number\,of\,incident\,photons} \times 100\%$$
$$= \frac{number\,of\,evloved\,CH_4\,molecules \times 8}{number\,of\,incident\,photons} \times 100\% \quad (1)$$

3. Results and discussion

The Pg-C$_3$N$_4$/Sn$_2$S$_3$-DETA hybrids are prepared by two-step route, as indicated in Fig. 1. When urea and sulfourea are mixed and heated, thiourea can be easily decomposited and large numbers of bubbles are formed. Meanwhile, the tris-s-triazine is come into being by re-arrangements of urea at high temperature. What's more, the sulfur species can be got rid of by raising the reaction temperature, which makes contribution to avoiding the introduction of impurities. In terms of Pg-C$_3$N$_4$, porous structures are appeared by the aggregation of tris-s-triazine unit around sulfur bubbles. The tris-s-triazine unit can be condensed to produce Pg-C$_3$N$_4$ sheets with leaving of sulfur bubbles. Then, the as-synthesized Pg-C$_3$N$_4$ are reacted with SnCl$_4$·5H$_2$O and thioacetamide in the mixed solution of DW and DETA at the temperature of 180 °C. The protonated organic molecules are incorporated into adjacent Sn$_2$S$_3$ layers by means of sulfur element. S, as nonmetal element, can be acted as matrix to modulate morphology, crystal size and performance of catalyst. In addition, Pg-C$_3$N$_4$ can easily couple with SnCl$_4$·5H$_2$O and thioacetamide to form Pg-C$_3$N$_4$/Sn$_2$S$_3$-DETA composites. Particularly, the inorganic-organic Sn$_2$S$_3$-DETA possesses more active spots, and Pg-C$_3$N$_4$ provides a substrate and easy way for the nucleation of Sn$_2$S$_3$, which contribute to increasing surface area and enlarge the heterostructured area between Pg-C$_3$N$_4$ and Sn$_2$S$_3$-DETA. Finally, the Pg-C$_3$N$_4$/Sn$_2$S$_3$-DETA composites are assembled by this method.

Fig. 2 shows XRD patterns of Sn$_2$S$_3$, Pg-C$_3$N$_4$/Sn$_2$S$_3$-DETA composites and Pg-C$_3$N$_4$ samples. The diffraction angles at 12.635°, 16.101°, 21.497°, 23.770°, 26.585°, 27.333°, 28.774°, 30.915°, 31.935°, 33.795°, 36.493°, 37.931°, 38.608°, 39.854°, 42.821°, 48.648°, 52.226°, 55.401° and 58.312° can be assigned to the (020), (120), (130), (220), (111), (140), (121), (310), (211), (221), (141), (250), (060), (160), (420), (440), (080), (530) and (540) crystal planes of Sn$_2$S$_3$ with an orthorhombic structure and the lines match well with reported values by JCPDS (No. 14-0619, a = 8.864 nm, b = 14.02 nm, c = 3.747 nm). For the pure Pg-C$_3$N$_4$, two remarkable diffraction peaks were discovered at
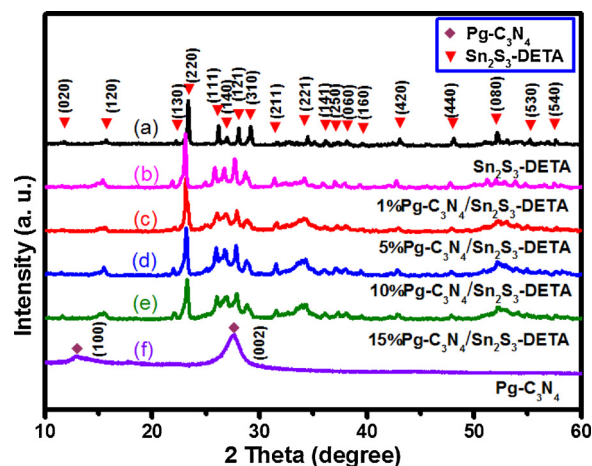

Fig. 2. XRD patterns of Pg-C$_3$N$_4$, Sn$_2$S$_3$-DETA and Pg-C$_3$N$_4$/Sn$_2$S$_3$-DETA photocatalysts.

appropriately 2θ = 13.204° and 27.496° which can be identified as (100) and (002) diffraction planes, respectively (JCPDS No. 87-1526). The strong peak at 2θ = 27.496°, corresponding to 0.325 nm interlayer distance. For Pg-C$_3$N$_4$/Sn$_2$S$_3$-DETA composite photocatalyst, no other characteristic peaks are detected, indicating high quality of as-fabricated powders.

Fig. 3a shows the TEM image of Pg-C$_3$N$_4$ and it is obvious that the Pg-C$_3$N$_4$ nanosheets have uniform and porous structure. Fig. 3b exhibits the HRTEM image of Sn$_2$S$_3$-DETA nanorods, which can be seen that the crystal size of Sn$_2$S$_3$-DETA gets well-controlled due to the introduction of diethylenetriamine. Besides, Fig. 3c displays the TEM image of Pg-C$_3$N$_4$/Sn$_2$S$_3$-DETA and it can be clearly seen that Pg-C$_3$N$_4$ nanosheets are covered by Sn$_2$S$_3$-DETA, which indicates perfect integration of Pg-C$_3$N$_4$ and Sn$_2$S$_3$-DETA. The HRTEM image of Sn$_2$S$_3$-DETA in Fig. 3d shows a clear heterojunction interface between Pg-C$_3$N$_4$ and Sn$_2$S$_3$-DETA and it also depicts the interplanar distance of Pg-C$_3$N$_4$ (0.325 nm) and Sn$_2$S$_3$ (0.335 nm), which can be assigned to (002) and (111) lattice plane, relatively. In addition, Fig. 3e–i exhibit elemental mapping figures of Pg-C$_3$N$_4$/Sn$_2$S$_3$-DETA, which reflects the presence of Sn, C, S and N elements.

Fig. 4 exhibits the complete XPS spectrum of C 1 s, Sn 3d, S 2p and N 1 s for the Pg-C$_3$N$_4$, Sn$_2$S$_3$-DETA and Pg-C$_3$N$_4$/Sn$_2$S$_3$-DETA composites, which investigate chemical surrounding of different elements near the sample surface range. As illustrated in Fig. 4a, the XPS survey spectra had peaks corresponding to element Sn, S, C and N, which is in
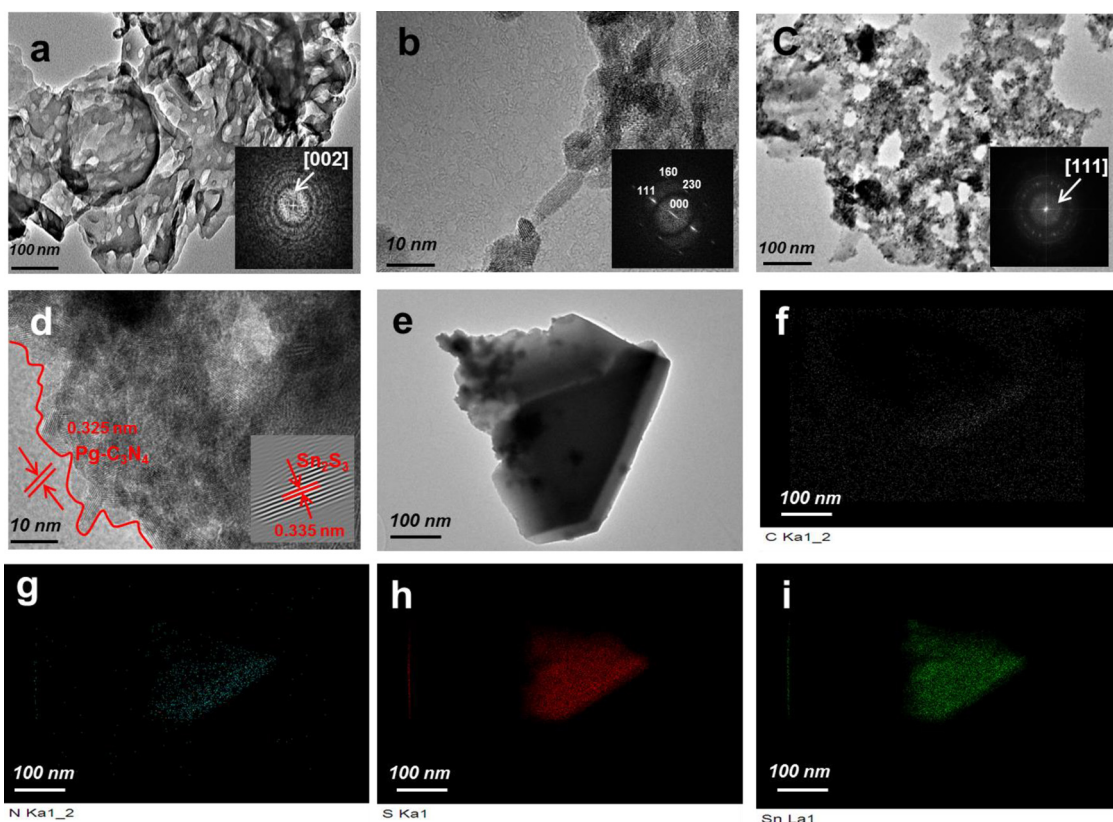
Fig. 3. (a)TEM image of Pg-C$_3$N$_4$ and its Fast Fourier Transformation pattern (inset), (b) HRTEM image of Sn$_2$S$_3$ and its Fast Fourier Transformation pattern (inset), (c) TEM image of Pg-C$_3$N$_4$/Sn$_2$S$_3$-DETA and its Fast Fourier Transformation pattern (inset), (d) HRTEM image of Pg-C$_3$N$_4$/Sn$_2$S$_3$-DETA, (e)TEM image with (f)-(i) corresponding elemental mapping images of Pg-C$_3$N$_4$/Sn$_2$S$_3$-DETA.

accordance with the TEM element mappings. As indicated in Fig. 4b, the main peaks for Sn 3d of Sn$_2$S$_3$ was detected at 494.60 and 486.13 eV, which can be indexed to Sn^{4+} and Sn^{2+} ions of Sn$_2$S$_3$, whereas for the spectra of the 5%Pg-C$_3$N$_4$/Sn$_2$S$_3$-DETA composite, the corresponding peak positions showed minor decreases to 494.16 and 485.69 eV. [56,57]. Fig. 4c exhibits S 2p peaks centered at 160.83 and 162.01 eV, as predicted for sulfide in Sn$_2$S$_3$, while the binding energies of spectra for 5%Pg-C$_3$N$_4$/Sn$_2$S$_3$-DETA composite shifted to 160.59 and 161.77 eV. Notably, both Sn 3d and S 2p for 5%Pg-C$_3$N$_4$/Sn$_2$S$_3$-DETA showed a minor shift to low value as compared to Sn$_2$S$_3$-DETA, implying the presence of electron transfer from Pg-C$_3$N$_4$ to Sn$_2$S$_3$-DETA after hybridization, which will be beneficial to build an internal electric field at the interface of the hybrid. For Pg-C$_3$N$_4$, C 1s spectrum can be divided to 2 peaks centered at 284.97 and 288.02 eV (Fig. 4d), which is attributed to sp^2-hybridized carbons and sp^2-bonded carbon in N-containing aromatic rings (N−C=N), respectively. The corresponding peak for 5%Pg-C$_3$N$_4$/Sn$_2$S$_3$-DETA composite was slightly shifted to 285.21 and 288.26 eV [58,59]. The peak at 284.72 eV can be attributed to DETA molecule[60]. As shown in Fig. 4e, N1 s spectrum of Pg-C$_3$N$_4$ can be fitted into 3 peaks and corresponding binding energies are 398.53, 399.12 and 401.16 eV. [61,62]. The first peak at 398.53 eV derives from sp^2-hybridized nitrogen (C–N=C) dominate in Pg-C$_3$N$_4$. The second peak at 399.12 eV is caused by the tertiary nitrogen N-(C)$_3$ groups, and last peak at 401.16 eV reveals the existence of amino groups (C−N−H) [63]. After combining with Sn$_2$S$_3$-DETA, the relevant binding energies all displayed slightly increases to 398.53, 399.53 and 400.83 eV, respectively. The peak at 398.79 eV is from DETA molecule [60]. The binding energies of C 1 s and N 1 s for 5%Pg-C$_3$N$_4$/Sn$_2$S$_3$-DETA showed a minor shift to high value compared to the Pg-C$_3$N$_4$, indicating the electron transfer from Pg-C$_3$N$_4$ to Sn$_2$S$_3$-DETA, which can further confirm the formation of build-in electric field and direct Z-scheme heterojunction between two components [64]. To a great

extent, these results perhaps indicate the good formation of a heterojunction by the in-situ growth of Sn$_2$S$_3$-DETA onto Pg-C$_3$N$_4$ nanosheets.

Surface area of as-fabricated photocatalysists is tested by N$_2$ gas adsorption-desorption procedures. Fig. 5a shows the adsorption-desorption curves and Fig. 5b summarizes BET surface area of Pg-C$_3$N$_4$/Sn$_2$S$_3$-DETA hybrids with different loading amounts of Pg-C$_3$N$_4$. Pg-C$_3$N$_4$ shows higher S$_{BET}$ than that of Sn$_2$S$_3$-DETA. Clearly, the introduction of Pg-C$_3$N$_4$ may result in the improvement of S$_{BET}$ of Pg-C$_3$N$_4$/Sn$_2$S$_3$-DETA. The obvious increase in S$_{BET}$ after loading Pg-C$_3$N$_4$ will be beneficial for enhancing surface active sites and photocatalytic activities.

The conventional unit cells of Sn$_2$S$_3$-DETA and Pg-C$_3$N$_4$ are shown in Fig. 6. To investigate the underlying electronic properties of Sn$_2$S$_3$-DETA and Pg-C$_3$N$_4$, the band structures along the high symmetry directions are calculated and shown in Fig. 7. The calculation results reflect that Sn$_2$S$_3$-DETA and Pg-C$_3$N$_4$ are indirect band gap semiconductor categories because their CBM and VBM locate at different high symmetry points (see Fig. 7). In general, the photogenerated charge carriers cannot recombine directly for indirect band gap semiconductors, which need the assistance of phonons to keep momentum conservation and very favorable for photocatalytic reaction [65]. In addition, the calculated band gaps of Sn$_2$S$_3$-DETA and Pg-C$_3$N$_4$ are 0.68 and 1.10 eV, respectively. It can be found that these calculation results are quite smaller than experimental results (2.14 eV for Sn$_2$S$_3$-DETA and 2.7 eV for Pg-C$_3$N$_4$ respectively). The reason can be explained as the main shortcoming of the GGA function in DFT calculations [66,67].

To further investigate the composition and nature of band structures, the DOS of Sn$_2$S$_3$-DETA and Pg-C$_3$N$_4$ are calculated and shown in Fig. 8. The upper VB and the CB of Sn$_2$S$_3$-DETA mainly consist of S 3p states and several Sn 5 s, 5p states. For Pg-C$_3$N$_4$, the upper VB is composed by N 2p states and several N 2 s states, and the CB mainly consists of C 2p states.
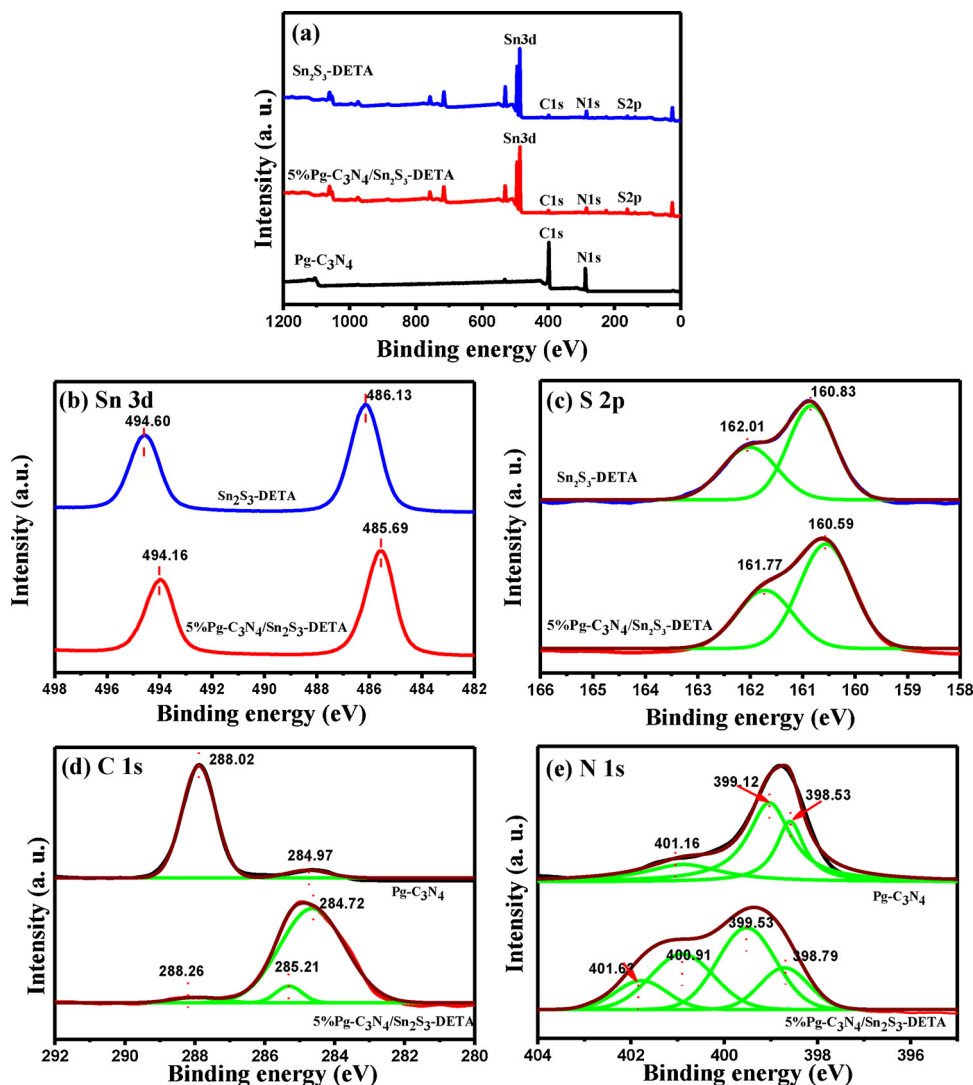
Fig. 4. XPS survey spectra of (a) Pg-C$_3$N$_4$, Sn$_2$S$_3$-DETA and 5%Pg-C$_3$N$_4$/Sn$_2$S$_3$-DETA, and high-resolution spectra of (b) Sn 3d, (c) S 2p, (d) C 1 s, and (e) N 1 s.
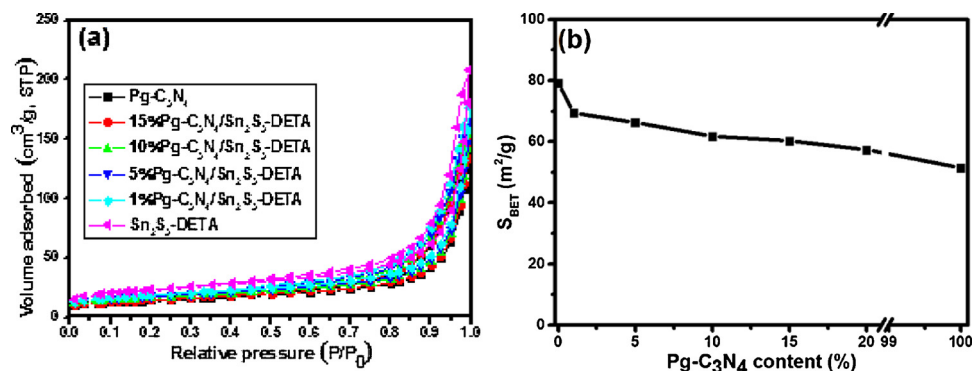

Fig. 5. (a) Isotherms for nitrogen adsorption-desorption and (b) S$_{BET}$ versus different Pg-C$_3$N$_4$ contents photocatalysts.

The optical performance of the catalysts is tested by UV–vis-NIR DRS. As indicated in Fig. 9a, Pg-C$_3$N$_4$ nanosheets and Sn$_2$S$_3$ nanorods exhibit an absorption edge at 443 and 579 nm, respectively. The curves of Pg-C$_3$N$_4$/Sn$_2$S$_3$-DETA are controlled by the weight ratio of Pg-C$_3$N$_4$ and Sn$_2$S$_3$-DETA and the composite structure. The color of different photocatalysts can be found in Fig. S2. According to the calculation in Fig. 7, Sn$_2$S$_3$-DETA and Pg-C$_3$N$_4$ are indirect band gap semiconductors. Fig. 9b is obtained from Fig. 9a according to experienced indirect band

gap formula 2 [54].

$$(Ah\nu)^{1/2} \sim h\nu - E_g \qquad (2)$$

A and *h*ν stand for absorbance and the energy of irradiation, respectively. According to Fig. 9b, E_g for Sn$_2$S$_3$-DETA and Pg-C$_3$N$_4$ is 2.14 and 2.62 eV, respectively.

The VB and CB potentials of a photocatalyst can be calculated as follows:

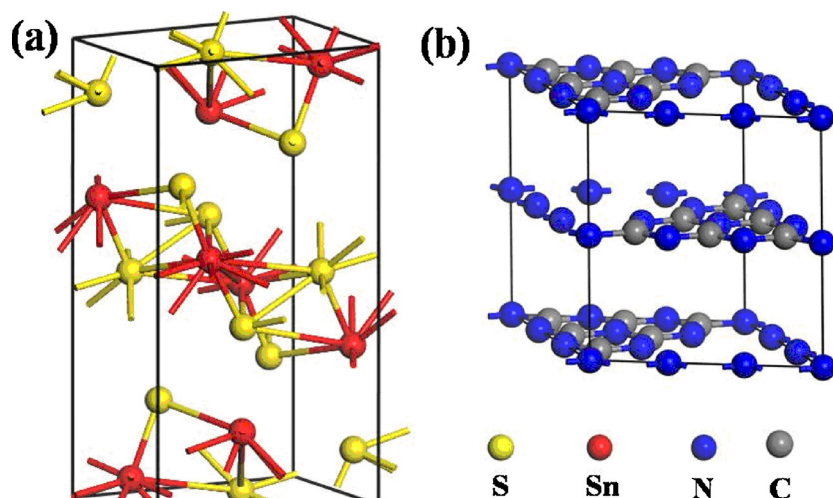**Fig. 6.** Schematic diagram of (a) Sn_2S_3-DETA and (b) Pg-C_3N_4 unit cell. (The S, Sn, N, C atoms are denoted by the yellow, red, blue and gray sphere, respectively.) (For interpretation of the references to colour in this figure legend, the reader is referred to the web version of this article).
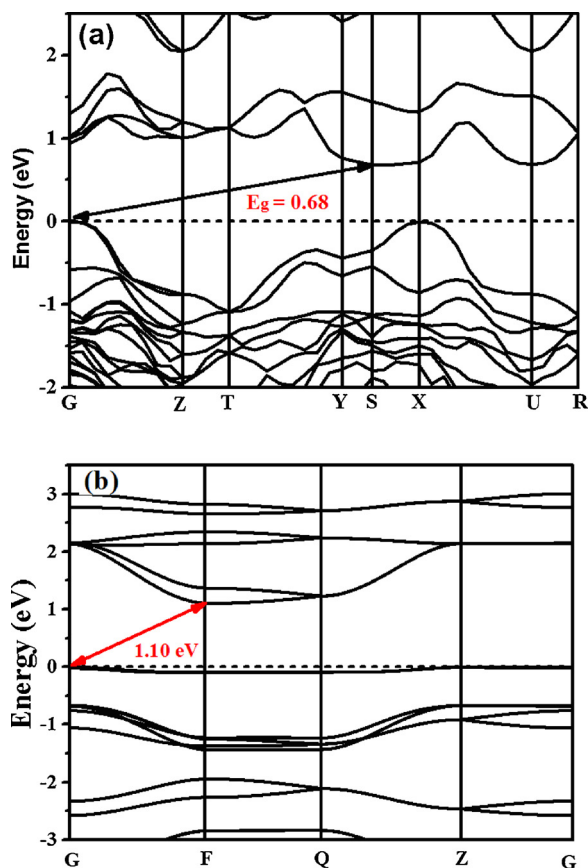

Fig. 7. The band structures for (a) Sn_2S_3-DETA and (b) Pg-C_3N_4.

Fig. 8. The DOS for (a) Sn_2S_3-DETA and (b) Pg-C_3N_4.

$$E_{VB} = X - E^e + 0.5E_g \qquad (3)$$

$$E_{CB} = E_{VB} - E_g \qquad (4)$$

Here, E^e is a constant (4.5 eV) and X is the electronegativity of semiconductor (X(Pg-C_3N_4) = 4.64 [68], X(Sn_2S_3) = 4.98 eV [69]). According to Eqs. (2–4), E_{CB} and E_{VB} for Pg-C_3N_4 are -1.17 and 1.45 eV. E_{CB} and E_{VB} for Sn_2S_3-DETA are -0.59 and 1.55 eV.

For the sake of determining the presence of different composites, Pg-C_3N_4, Pg-C_3N_4/Sn_2S_3-DETA and Sn_2S_3-DETA are investigated by the FT-IR spectroscope in Fig. 10. In terms of Pg-C_3N_4/Sn_2S_3-DETA, the peak at
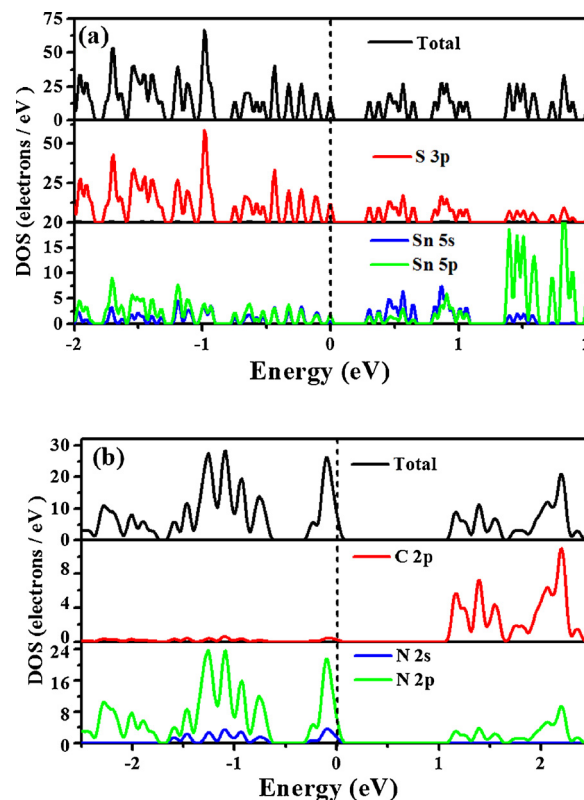
1331 and 1463 cm^{-1} match the typical stretching modes of C−N heterocycles [70]. In addition, a typical breathing of s-triazine at 803 cm^{-1} is tested. This expounds the presence of Pg-C_3N_4 in the Pg-C_3N_4/Sn_2S_3-DETA composite. The absorption feature of Sn_2S_3-DETA centered at 961 cm^{-1} is attributed to Sn-S stretching mode. As for Pg-C_3N_4/Sn_2S_3-DETA composites, a small amount of red shift of the 806 cm^{-1} characteristic peak can be found, which suggests that there was an obvious combination between Pg-C_3N_4 and Sn_2S_3-DETA. thus, Pg-C_3N_4 and Sn_2S_3-DETA have coupled together successfully.

The charge separation and transmission of the semiconductor can be investigated through PL instrument. Fig. 11 shows PL spectra of Pg-C_3N_4, Sn_2S_3-DETA and Pg-C_3N_4/Sn_2S_3-DETA nanocomposites at the
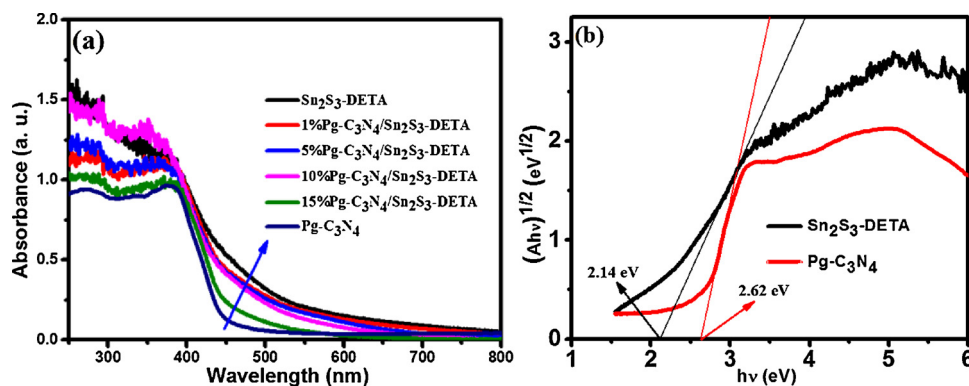
Fig. 9. (a) UV–vis DRS spectra of as-prepared samples, (b) plots of $(Ah\nu)^{1/2}$ versus energy ($h\nu$) of Pg-C_3N_4 and Sn_2S_3.
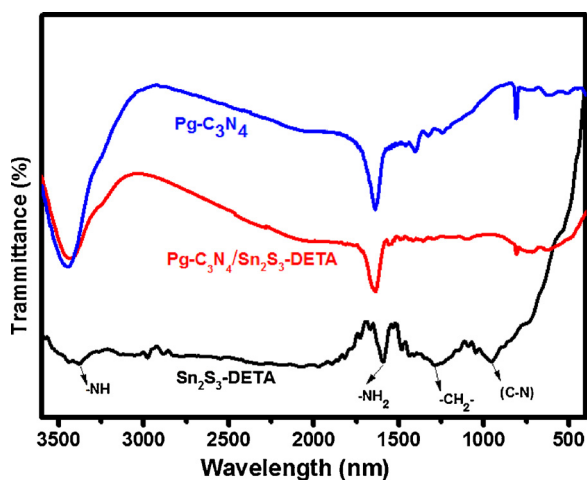

Fig. 10. FT-IR spectra of Pg-C_3N_4, Pg-C_3N_4/Sn_2S_3-DETA, and Sn_2S_3-DETA.
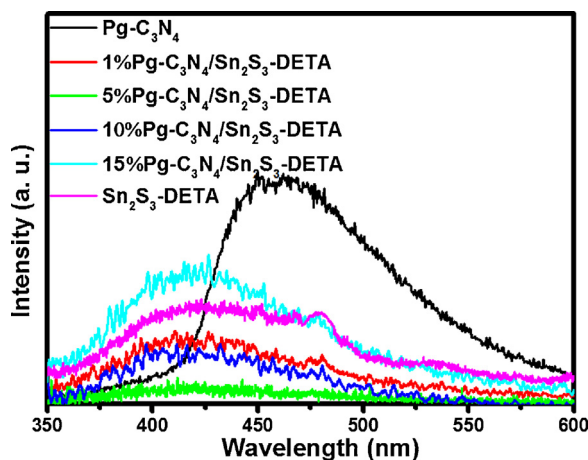
Fig. 11. PL spectra of Pg-C_3N_4, Sn_2S_3-DETA and Pg-C_3N_4/Sn_2S_3-DETA composite.

room temperature with an excitation of 325 nm light irradiation. Compared to pure Pg-C_3N_4, Pg-C_3N_4/Sn_2S_3-DETA nanocomposites have reduced PL intensity. This is attributed to the formation of the heterojunction between Sn_2S_3-DETA and Pg-C_3N_4, which indicates that a high charge separation and transmission rate of photoexcited e$^-$ and h$^+$ can be efficiently enforced owing to the introduced Pg-C_3N_4, further resulting in conspicuous enhanced photocatalysis efficiency of as-fabricated Pg-C_3N_4/Sn_2S_3-DETA. As it can be seen from Fig. 11, the 5%Pg-C_3N_4/Sn_2S_3-DETA shows the lowest PL intensity, which indicates the reduction in recombination of e$^-$ and h$^+$. As above discussed, 5%Pg-

C_3N_4/Sn_2S_3-DETA shows the highest catalytic performance. It can be found that PL spectra results are in accordance with PCR activity. Thus, the efficient separation of photoinduced e$^-$ and h$^+$ make great contributions to enhancing photocatalytic activity of semiconductors.

In order to further comprehend catalytic enhancement mechanism for CO_2 photoreduction, the separation and transmission for photogenerated electron and hole pairs were tested by photoelectrochemical method. A phenomenon commonly occurs in this way: the stronger the photocurrent is, the faster e$^-$ and h$^+$ separate. Fig. 12 exhibits the photocurrent-time curves of Pg-C_3N_4, Sn_2S_3-DETA and Pg-C_3N_4 with two on-off intermittent irradiation cycles at 0.5 V potential condition. It is obvious that 5%Pg-C_3N_4/Sn_2S_3-DETA shows the highest photocurrent density as compared to pure Pg-C_3N_4, Sn_2S_3-DETA and other Pg-C_3N_4/Sn_2S_3-DETA composites, indicating that proper amount of Pg-C_3N_4 could remarkably separate interfacial photo-excited electron-hole pairs between Pg-C_3N_4 and Sn_2S_3-DETA, which makes great contributions to photoactivity enhancement.

The PCR performance for as-obtained samples was investigated under visible light excitation (λ > 420 nm). Fig. 13a shows photocatalytic CH_4 and CH_3OH production rate of Pg-C_3N_4, Pg-C_3N_4/Sn_2S_3-DETA nanocomposites and Sn_2S_3-DETA under identical conditions. As for Sn_2S_3-DETA, it exhibits poor photocatalytic performance due to the easy recombination of photoexcited carriers. Although the photocatalytic CH_4 and CH_3OH production rate for pure Sn_2S_3-DETA can be intuitively seen from Fig. 13a, the photocatalytic activity is far more away from the idea standard. However, Pg-C_3N_4/Sn_2S_3-DETA heterostructures exhibits a much higher activity of CH_4 and CH_3OH production than pure Pg-C_3N_4 and Sn_2S_3-DETA alone. With the growth of Pg-C_3N_4 content, the CH_4 and CH_3OH production rate grows gradually, and 5%Pg-C_3N_4/Sn_2S_3-DETA nanocomposite shows much higher CH_4-production rate of appropriate $4.84\,\mu mol\,h^{-1}\,g^{-1}$ and CH_3OH-
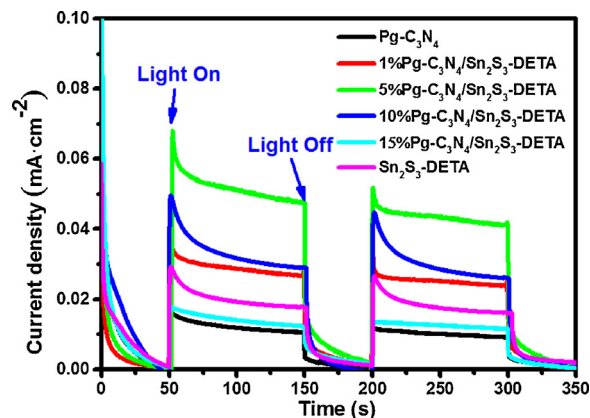

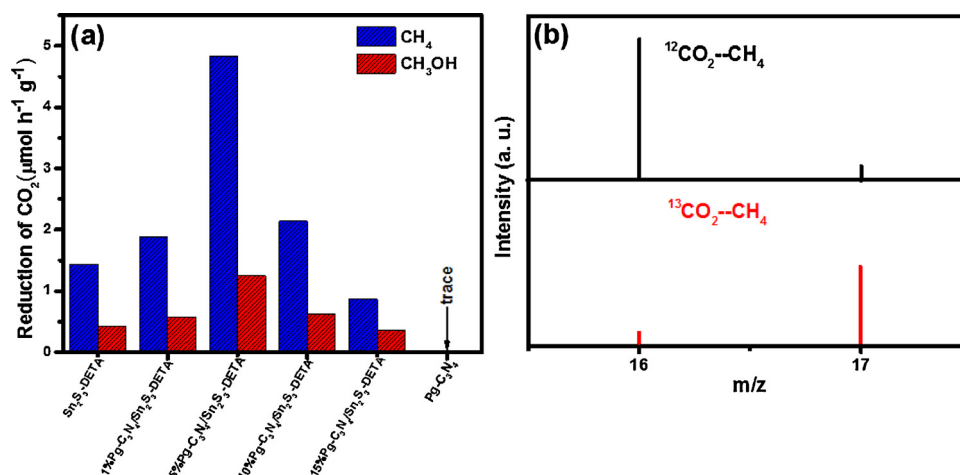**Fig. 12.** Transient photocurrent responses (I-t curves) of different photocatalysts.

Fig. 13. (a) Comparison of the PCR rate of different photocatalysts under visible light irradiation and (b) The GC–MS patterns of the produced CH_4 over 5%Pg-C_3N_4/Sn_2S_3-DETA using $^{12}CO_2$ and $^{13}CO_2$ as the carbon source, respectively.

production rate of appropriate 1.35 μmol h^{-1} g^{-1}, and the QE of 5%Pg-C_3N_4/Sn_2S_3-DETA nanocomposite is 2.8%. Nevertheless, with a persistent increase of Pg-C_3N_4, the CH_4 and CH_3OH production rate decreases rapidly. PCR performance was also confirmed by changing 4 M HCl to 2 M H_2SO_4. As indicted in Fig. S3, CH_4-production rate of 4.93 μmol h^{-1} g^{-1} and CH_3OH-production rate of 1.49 μmol h^{-1} g^{-1} are obtained by 5%Pg-C_3N_4/Sn_2S_3-DETA composite. Thus, the HCl or Cl- will not take part into the photocatalytic reactions. In order to further verify the real carbon source of photocatalytic products, the isotopic $^{13}CO_2$ is used as the reactant to trace the carbon sources in the photocatalytic reaction and $^{12}CO_2$ was also tested as the reference, the obtained products were identified by the GC–MS. As illustrated in Fig. 13b, GC–MS analysis indicates that $^{12}CH_4$ ($m/z = 16$) is the principle product with $^{12}CO_2$ as the carbon source, while $^{13}CH_4$ ($m/z = 17$) with $^{13}CO_2$ is the principle product with $^{13}CO_2$ as the carbon source. Therefore, it is obvious that the detected products over the as-fabricated samples originated from CO_2 source rather than any other carbon species.

The photostability of catalysts is of great concern for industrial application. To exhibit the photostability of 5%Pg-C_3N_4/Sn_2S_3-DETA, we implement 3 recycling experiments under the same conditions. As indicated in Fig. 14, the CH_4 and CH_3OH production of 5%Pg-C_3N_4/Sn_2S_3-DETA remains almost unchanged after three cycling times, indicating the high photostability of 5%Pg-C_3N_4/Sn_2S_3-DETA composite.

In order to further investigate the PCR process, *in situ* FT-IR has been implemented to detect the CO_2 conversion intermediates over the 5% Pg-C_3N_4/Sn_2S_3-DETA composite. The spectrum of 5%Pg-C_3N_4/Sn_2S_3-

DETA was first recorded as background without CO_2 introduction and irradiation. After introducing CO_2, the following obtained spectrum was subtracted the background. At the first 60 min, CO_2 absorption was conducted on the 5%Pg-C_3N_4/Sn_2S_3-DETA composite under the continuous flow of H_2O vapor and CO_2. As indicated on Fig. 15, the peaks at 1648, 1620, 1541, 1511, 1425 and 1287 cm^{-1} are attributed to carbonate species. In particular, most peaks display a minor enhancement on the position change under irradiation. The peaks centered at 1745, 1713, 1685, 1579, 1558, 1397 and 1339 cm^{-1} are ascribed to formate (HCOO) and the peaks observed at 1772, 1730, 1671, 1605, 1473 and 1240 cm^{-1} can be assigned to formaldehyde (HCHO). Moreover, the peaks at 1701 and 1459 cm^{-1} are ascribed to the stretching vibration of methoxyl groups (CH$_3$O). However, CH_4 was not detected due to its nonpolar property and poor affinity on 5%Pg-C_3N_4/Sn_2S_3-DETA surface. These results distinctly show that only carbonate species can be found before irradiation with flowing CO_2 and H_2O vapor. After light irradiation, formate species, formaldehyde and methoxyl groups could be gradually detected, which indicate that photocatalytic conversion CO_2 to CH_4 and CH_3OH on 5%Pg-C_3N_4/Sn_2S_3-DETA is a multi-step process.

The optimized structures and the calculated average potential profile of Sn_2S_3 (1 1 1) crystal plane and monolayer g-C_3N_4 are shown in
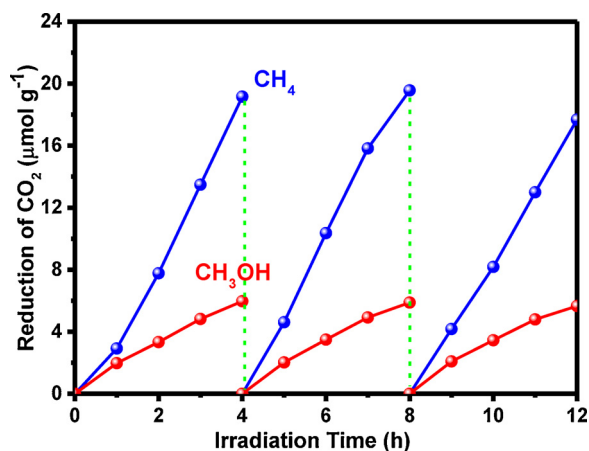

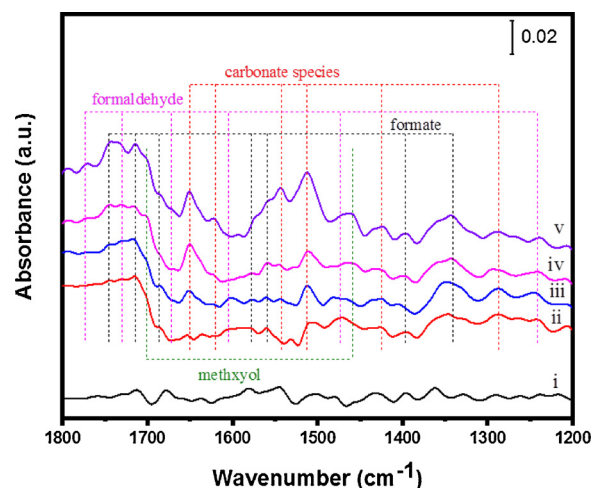**Fig. 14.** Photocatalytic stability of 5%Pg-C_3N_4/Sn_2S_3-DETA.

Fig. 15. *In situ* FT-IR spectra of 5%Pg-C_3N_4/Sn_2S_3-DETA under different conditions: (i) without introducing CO_2 gas and irradiation, (ii) flowing CO_2 gas for 30 min and without irradiation, (iii) flowing CO_2 gas for 60 min and without irradiation, (iv) irradiation for 30 min and (v) 60 min.
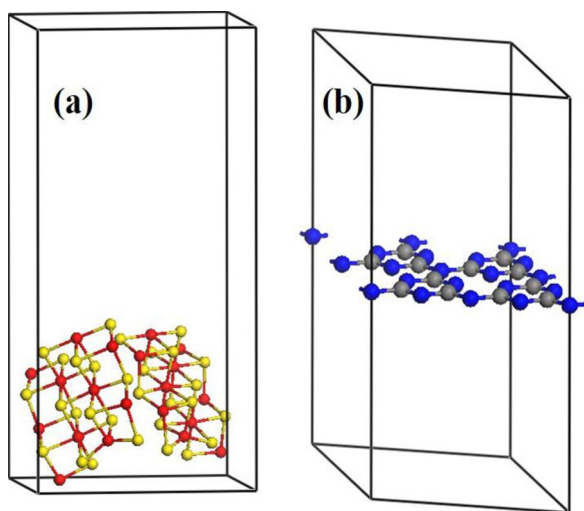
Fig. 16. Optimized structures of (a) Sn_2S_3 (1 1 1) crystal plane and (b) monolayer g-C_3N_4. The yellow red, blue and gray spheres are S, Sn, N and C atoms, respectively. (For interpretation of the references to colour in this figure legend, the reader is referred to the web version of this article).
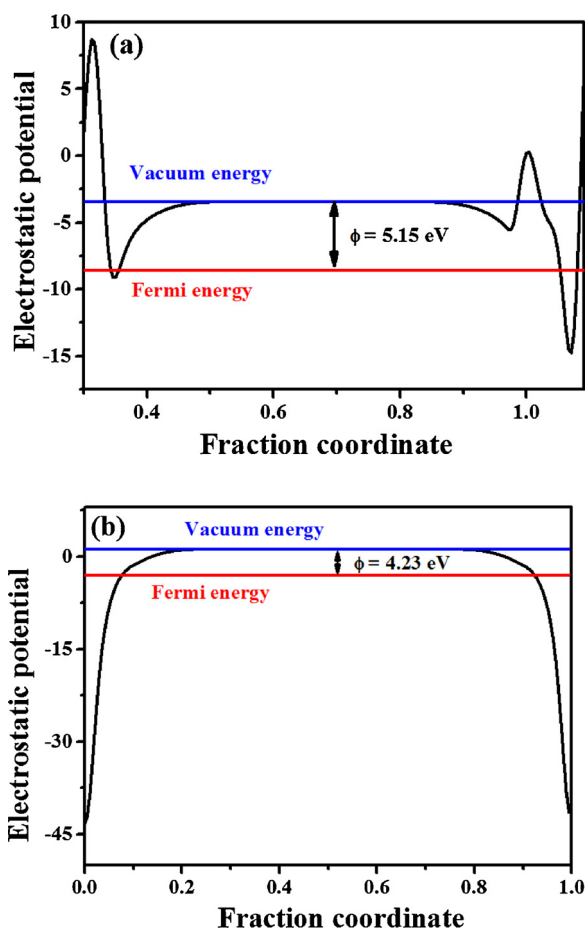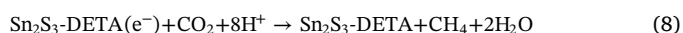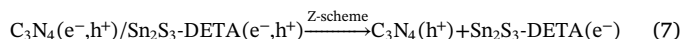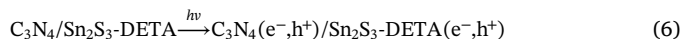

Fig. 17. Calculated electrostatic potentials of (a) (1 1 1) facet of Sn_2S_3 and (b) monolayer g-C_3N_4.

Figs. 16 and 17, respectively. The Fermi energy of the semiconductor is important parameter in estimating the charge transmission between the surfaces of two catalysts. Moreover, the Fermi energy can be calculated by the following equation:

$$\Phi = E_{vac} - E_F \tag{5}$$

Where E_{vac} and E_F are lectrostatic potential of the vacuum energy and Fermi energy, respectively. The calculated work functions of Sn_2S_3 (1 1 1) facet and monolayer g-C_3N_4 were 5.15 and 4.23 eV, respectively. The Fermi energy of g-C_3N_4 is higher than that of Sn_2S_3. During the establishment the semiconductor compound of Sn_2S_3 (1 1 1) facet and monolayer g-C_3N_4, electrons will transmit from g-C_3N_4 to Sn_2S_3 until their Fermi energies reach the same level, which leads to the decrease of electron density of g-C_3N_4 and an increase in Sn_2S_3, implying the formation of built-in electric field (IEF) between the interface of Sn_2S_3 and g-C_3N_4, and the direction of IEF is from g-C_3N_4 surface to Sn_2S_3 surface, which was beneficial to the diffusion and separation of photoirradiated e^- and h^+ pairs. This calculation further confirms the generation of the Z-scheme heterostructure between Pg-C_3N_4 and Sn_2S_3-DETA.

Z-scheme photocatalytic mechanism of Pg-C_3N_4/Sn_2S_3-DETA heterostructure is provisionally proposed in Fig. 18. And it can help us understand the charge transfer processes preferably. Band edge positions of Pg-C_3N_4 and Sn_2S_3-DETA are also presented in Fig. 18. As described above, E_g of Sn_2S_3-DETA and Pg-C_3N_4 is 2.14 and 2.62 eV, respectively. E_{CB} of Pg-C_3N_4 and Sn_2S_3-DETA is -1.17 and -0.59 V vs. NHE (pH = 7), respectively, which is lower than reduction potentials of CO_2 to CH_4. Therefore, in terms of thermodynamic viewpoint, both semiconductors have the ability to be photoexcited and then reduce CO_2 to CH_4 and CH_3OH. When irradiated by visible light, e^--h^+ pairs are photogenerated in Pg-C_3N_4 and Sn_2S_3-DETA. The photoexcited h^+ probably remain in Sn_2S_3-DETA VB, whereas the e- in Sn_2S_3-DETA CB transfers to VB of Pg-C_3N_4 due to ohmic contact. The e- in Pg-C_3N_4 VB is further stimulated to its CB, which is beneficial to improve the efficiency towards the separation of e^--h^+ pairs. The h^+ stored in Sn_2S_3-DETA VB is trapped in H_2O molecule to produce H^+ and O_2. Simultaneously, the e- in Pg-C_3N_4 CB is transmitted to its surface, which can increase the e- density of Pg-C_3N_4. CH_4 formation requires 8 electrons [71]. The enriched e- ions on surface of Pg-C_3N_4 are likely to urge CO_2 reduction and CH_4 formation. Therefore, the Z-scheme heterostructure has improved the performance of photocatalytic conversion CO_2 to CH_4, not only can it promote the efficient separation of e^--h^+ pairs [72], but enhance the redox potential of photocatalyst [73]. In terms of Z-scheme structure, it can enlarge lifetime of e^--h^+ pairs and improve redox potential, which result in efficient separation of charge carriers and enhancement of photoreduction CO_2. In addition, the structure of Sn_2S_3-DETA and Pg-C_3N_4 with large contact surface and strong bond strength can also hinder recombination of photoexcited e^--h^+ pairs. In the reaction process, we provide an environment with high concentrated CO_2 on the catalyst surface, which can accelerate the reaction with photoinduced e- and promote the PCR performance. The major photoreaction steps can be summarized in the following reactions:

$$C_3N_4/Sn_2S_3\text{-DETA} \xrightarrow{h\nu} C_3N_4(e^-,h^+)/Sn_2S_3\text{-DETA}(e^-,h^+) \tag{6}$$

$$C_3N_4(e^-,h^+)/Sn_2S_3\text{-DETA}(e^-,h^+) \xrightarrow{Z\text{-scheme}} C_3N_4(h^+)+Sn_2S_3\text{-DETA}(e^-) \tag{7}$$

$$Sn_2S_3\text{-DETA}(e^-)+CO_2+8H^+ \rightarrow Sn_2S_3\text{-DETA}+CH_4+2H_2O \tag{8}$$

4. Conclusion

In summary, we have successfully in-situ controlled Sn_2S_3-DETA nanorods on Pg-C_3N_4 nanosheets surface to fabricate a new Z-scheme Pg-C_3N_4/Sn_2S_3-DETA composite photocatalyst by using a simple small-molecule-amine-assisted hydrothermal strategy. This easily obtained and earth-abundant catalyst displayed higher photocatalytic activity for CO_2 reduction into CH_4 and CH_3OH than bulk Pg-C_3N_4 and considerable photostability, which is distributed to the higher specific surface area, better light harvesting, greater CO_2 consum capacity and forceful photoinduced e^--h^+ separation. In this work, Pg-C_3N_4/Sn_2S_3-DETA nanocomposites are a very promising candidate for possible practical application in high performance photoreduction CO_2. In addition, the
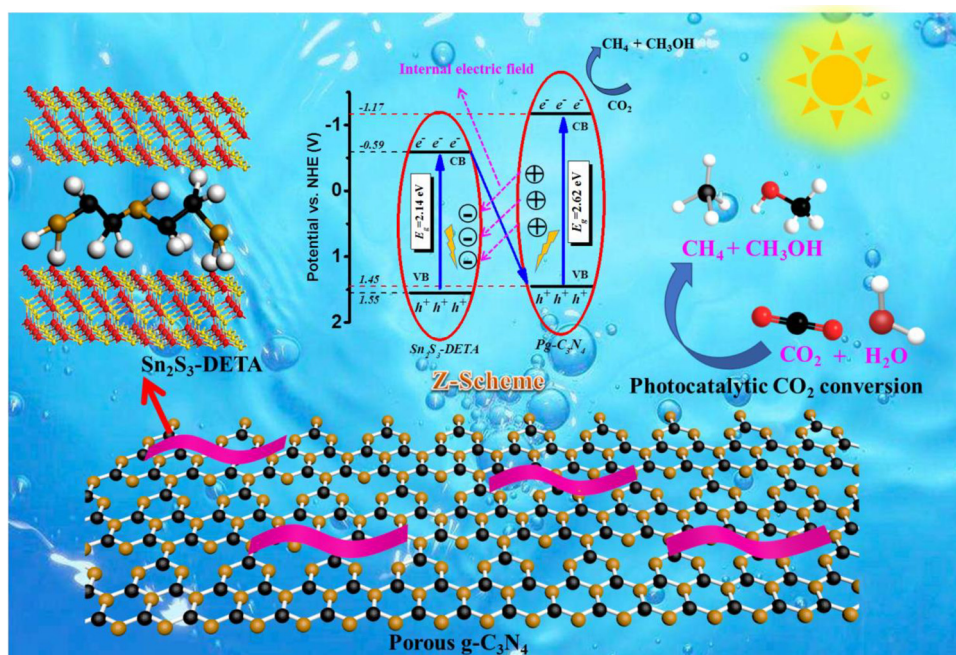
Fig. 18. Schematic representation of Pg-C₃N₄/Sn₂S₃-DETA system. s.

proposed mechanisms for PCR process may also provide new ideas for the future design of new photocatalyst and can be used in the field of solar-fuel conversion.

Appendix A. Supplementary data

Supplementary material related to this article can be found, in the online version, at doi:https://doi.org/10.1016/j.apcatb.2018.09.073.

References

[1] W. Wang, M.O. Tade, Z. Shao, Research progress of perovskite materials in photocatalysis- and photovoltaics-related energy conversion and environmental treatment, Chem. Soc. Rev. 44 (2015) 5371–5408.
[2] Z. Zhou, Y. Zhang, Y. Shen, S. Liu, Y. Zhang, Molecular engineering of polymeric carbon nitride: advancing applications from photocatalysis to biosensing and more, Chem. Soc. Rev. 47 (2018) 2298–2321.
[3] J.X. Low, J.G. Yu, M. Jaroniec, S. Wageh, A.A. Al-Ghamdi, Heterojunction Photocatalysts, Adv. Mater. 29 (2017) 1601694.
[4] M.-H. Sun, S.-Z. Huang, L.-H. Chen, Y. Li, X.-Y. Yang, Z.-Y. Yuan, B.-L. Su, Applications of hierarchically structured porous materials from energy storage and conversion, catalysis, photocatalysis, adsorption, separation, and sensing to biomedicine, Chem. Soc. Rev. 45 (2016) 3479–3563.
[5] T. Nakajima, Y. Tamaki, K. Ueno, E. Kato, T. Nishikawa, K. Ohkubo, Y. Yamazaki, T. Morimoto, O. Ishitani, Photocatalytic reduction of low concentration of CO₂, J. Am. Chem. Soc. 138 (2016) 13818–13821.
[6] T. Zhang, J. Low, K. Koh, J. Yu, T. Asefa, Mesoporous TiO₂ comprising small, highly crystalline nanoparticles for efficient CO₂ reduction by H₂O, ACS Sustain. Chem. Eng. 6 (2018) 531–540.
[7] J. Low, B. Cheng, J. Yu, Surface modification and enhanced photocatalytic CO₂ reduction performance of TiO₂: a review, Appl. Surf. Sci. 392 (2017) 658–686.
[8] F. Li, L. Zhang, X. Chen, Y.L. Liu, S.G. Xu, S.K. Cao, Synergistically enhanced photocatalytic reduction of CO₂ on N-Fe codoped BiVO₄ under visible light irradiation, Phys. Chem. Chem. Phys. 19 (2017) 21862–21868.
[9] J. Mao, T. Peng, X. Zhang, K. Li, L. Zan, Selective methanol production from photocatalytic reduction of CO₂ on BiVO₄ under visible light irradiation, Catal.
Commun. 28 (2012) 38–41.
[10] Q. Liu, Y. Zhou, J. Kou, X. Chen, Z. Tian, J. Gao, S. Yan, Z. Zou, High-yield synthesis of ultralong and ultrathin Zn₂GeO₄ nanoribbons toward improved photocatalytic reduction of CO₂ into renewable hydrocarbon fuel, J. Am. Chem. Soc. 132 (2010) 14385–14387.
[11] H. Zhao, X. Wang, J. Feng, Y. Chen, X. Yang, S. Gao, R. Cao, Synthesis and characterization of Zn₂GeO₄/Mg-MOF-74 composites with enhanced photocatalytic activity for CO₂ reduction, Cataly. Sci. Technol. 8 (2018) 1288–1295.
[12] Y. Fu, D. Sun, Y. Chen, R. Huang, Z. Ding, X. Fu, Z. Li, An amine-functionalized titanium metal-organic framework photocatalyst with visible-light-induced activity for CO₂ reduction, Angew. Chem. Int. Ed. Engl. 51 (2012) 3364–3367.
[13] A. Dhakshinamoorthy, Z. Li, H. Garcia, Catalysis and photocatalysis by metal organic frameworks, Chem. Soc. Rev. (2018), https://doi.org/10.1039/c1038cs00256h.
[14] Y. Chen, D. Wang, X. Deng, Z. Li, Metal–organic frameworks (MOFs) for photocatalytic CO₂ reduction, Catal. Sci. Technol. 7 (2017) 4893–4904.
[15] Y.-F. Xu, M.-Z. Yang, B.-X. Chen, X.-D. Wang, H.-Y. Chen, D.-B. Kuang, C.-Y. Su, A CsPbBr₃ perovskite quantum Dot/Graphene oxide composite for photocatalytic CO₂ reduction, J. Am. Chem. Soc. 139 (2017) 5660–5663.
[16] H. Jiang, K.-i. Katsumata, J. Hong, A. Yamaguchi, K. Nakata, C. Terashima, N. Matsushita, M. Miyauchi, A. Fujishima, Photocatalytic reduction of CO₂ on Cu₂O-loaded Zn-Cr layered double hydroxides, Appl. Catal. B: Environ. 224 (2018) 783–790.
[17] S. Cao, Y. Li, B. Zhu, M. Jaroniec, J. Yu, Facet effect of Pd cocatalyst on photocatalytic CO₂ reduction over g-C₃N₄, J. Catal. 349 (2017) 208–217.
[18] Y. Wang, N.-Y. Huang, J.-Q. Shen, P.-Q. Liao, X.-M. Chen, J.-P. Zhang, Hydroxide ligands cooperate with catalytic centers in metal-organic frameworks for efficient photocatalytic CO₂ reduction, J. Am. Chem. Soc. 140 (2018) 38–41.
[19] K.K. Ghuman, L.B. Hoch, P. Szymanski, J.Y.Y. Loh, N.P. Kherani, M.A. E-Sayed, G.A. Ozin, C.V. Singh, Photoexcited Surface Frustrated Lewis Pairs for Heterogeneous Photocatalytic CO₂ Reduction, J. Am. Chem. Soc. 138 (2016) 1206–1214.
[20] J. Yu, J. Low, W. Xiao, P. Zhou, M. Jaroniec, Enhanced photocatalytic CO₂-reduction activity of anatase TiO₂ by coexposed {001} and {101} Facets, J. Am. Chem. Soc. 136 (2014) 8839–8842.
[21] J. Ran, M. Jaroniec, S.-Z. Qiao, Cocatalysts in semiconductor-based photocatalytic co₂ reduction: achievements, challenges, and opportunities, Adv. Mater. 30 (2018) 1704649.
[22] T. Zhang, W. Lin, Metal-organic frameworks for artificial photosynthesis and photocatalysis, Chem. Soc. Rev. 43 (2014) 5982–5993.
[23] M.F. Kuehnel, K.L. Orchard, K.E. Dalle, E. Reisner, Selective photocatalytic CO₂ Reduction in water through anchoring of a molecular Ni catalyst on CdS nanocrystals, J. Am. Chem. Soc. 139 (2017) 7217–7223.
[24] B. Zhu, L. Zhang, B. Cheng, J. Yu, First-principle calculation study of tri-s-triazine-based g-C₃N₄: A review, Appl. Catal. B: Environ. 224 (2018) 983–999.
[25] K. Wang, G. Zhang, J. Li, Y. Li, X. Wu, OD/2D Z-Scheme heterojunctions of bismuth tantalate quantum dots/ultrathin g-C₃N₄ nanosheets for highly efficient visible light photocatalytic degradation of antibiotics, ACS Appl. Mater. Interfaces 9 (2017) 43704–43715.
[26] J. Fu, J. Yu, C. Jiang, B. Cheng, g-C₃N₄-Based heterostructured photocatalysts, Adv. Energy Mater. 8 (2018) 1701503.

[27] Z. Sun, H. Wang, Z. Wu, L. Wang, g-C₃N₄ based composite photocatalysts for photocatalytic CO₂ reduction, Catal. Today 300 (2018) 160–172.

[28] J. Fu, B. Zhu, C. Jiang, B. Cheng, W. You, J. Yu, Hierarchical porous O-Doped g-C₃N₄ with enhanced photocatalytic CO₂ reduction activity, Small 13 (2017) 1603938.

[29] Z. Jiang, W. Wan, H. Li, S. Yuan, H. Zhao, P.K. Wong, A hierarchical Z-Scheme alpha-Fe₂O₃/g-C₃N₄ hybrid for enhanced photocatalytic CO₂ reduction, Adv. Mater. 30 (2018) 1706108.

[30] J. Barber, Photosynthetic energy conversion: natural and artificial, Chem. Soc. Rev. 38 (2009) 185–196.

[31] K. Sekizawa, K. Maeda, K. Domen, K. Koike, O. Ishitani, Artificial Z-Scheme constructed with a supramolecular metal complex and semiconductor for the photocatalytic reduction of CO₂, J. Am. Chem. Soc. 135 (2013) 4596–4599.

[32] J. Lv, J. Zhang, J. Liu, Z. Li, K. Dai, C. Liang, Bi SPR-promoted Z-scheme Bi₂MoO₆/CdS-diethylenetriamine composite with effectively enhanced visible light photocatalytic hydrogen evolution activity and stability, ACS Sustain. Chem. Eng. 6 (2018) 696–706.

[33] L.J. Zhang, S. Li, B.K. Liu, D.J. Wang, T.F. Xie, Highly efficient CdS/WO₃ photocatalysts: Z-scheme photocatalytic mechanism for their enhanced photocatalytic h₂ evolution under visible light, ACS Catal. 4 (2014) 3724–3729.

[34] L. Zou, H. Wang, X. Wang, High efficient photodegradation and photocatalytic hydrogen production of CdS/BiVO₄ heterostructure through Z-scheme process, ACS Sustain. Chem. Eng. 5 (2017) 303–309.

[35] R. Ye, H. Fang, Y.-Z. Zheng, N. Li, Y. Wang, X. Tao, Fabrication of CoTiO₃/g-C₃N₄ hybrid photocatalysts with enhanced H₂ evolution: Z-scheme photocatalytic mechanism insight, ACS Appl. Mater. Interfaces 8 (2016) 13879–13889.

[36] W. Li, C. Feng, S. Dai, J. Yue, F. Hua, H. Hou, Fabrication of sulfur-doped g-C₃N₄/Au/CdS Z-scheme photocatalyst to improve the photocatalytic performance under visible light, Appl. Catal. B: Environ. 168 (2015) 465–471.

[37] M. Zhu, Z. Sun, M. Fujitsuka, T. Majima, Z-scheme photocatalytic water splitting on a 2D heterostructure of black phosphorus/bismuth vanadate using visible light, Angew. Chem. Int. Ed. 57 (2018) 2160–2164.

[38] T. Di, B. Zhu, B. Cheng, J. Yu, J. Xu, A direct Z-scheme g-C₃N₄/SnS₂ photocatalyst with superior visible-light CO₂ reduction performance, J. Catal. 352 (2017) 532–541.

[39] Q.C. Yuan, D. Liu, N. Zhang, W. Ye, H.X. Ju, L. Shi, R. Long, J.F. Zhu, Y.J. Xiong, Noble-metal-Free janus-like structures by cation exchange for Z-scheme photocatalytic water splitting under broadband light irradiation, Angew. Chem. Int. Ed. 56 (2017) 4206–4210.

[40] Z. Wang, J. Lv, J. Zhang, K. Dai, C. Liang, Facile synthesis of Z-scheme BiVO₄/porous graphite carbon nitride heterojunction for enhanced visible-light-driven photocatalyst, Appl. Surf. Sci. 430 (2018) 595–602.

[41] J. Lv, K. Dai, J. Zhang, Q. Liu, C. Liang, G. Zhu, Facile constructing novel 2D porous g-C₃N₄/BiOBr hybrid with enhanced visible-light-driven photocatalytic activity, Sep. Purif. Technol. 178 (2017) 6–17.

[42] J. Zhang, J. Lv, K. Dai, Q. Liu, C. Liang, G. Zhu, Facile and green synthesis of novel porous g-C₃N₄/Ag₃PO₄ composite with enhanced visible light photocatalysis, Ceram. Int. 43 (2017) 1522–1529.

[43] Z. Zhang, Y. Zhang, L. Lu, Y. Si, S. Zhang, Y. Chen, K. Dai, P. Duan, L. Duan, J. Liu, Graphitic carbon nitride nanosheet for photocatalytic hydrogenproduction The impact of morphology and element composition, Appl. Surf. Sci. 391 (2017) 369–375.

[44] K.C. Christoforidis, A. Sengele, V. Keller, N. Keller, Single-step synthesis of SnS₂ nanosheet-decorated TiO₂ anatase nanofibers as efficient photocatalysts for the degradation of gas-phase diethylsulfide, ACS Appl. Mater. Interfaces 7 (2015) 19324–19334.

[45] T.M. Suzuki, T. Takayama, S. Sato, A. Iwase, A. Kudo, T. Morikawa, Enhancement of CO₂ reduction activity under visible light irradiation over Zn-based metal sulfides by combination with Ru-complex catalysts, Appl. Catal. B: Environ. 224 (2018) 572–578.

[46] Y. Yu, Y. Huang, Y. Yu, Y. Shi, B. Zhang, Design of continuous built-in band bending in self-supported CdS nanorod-based hierarchical architecture for efficient photoelectrochemical hydrogen production, Nano Energy 43 (2018) 236–243.

[47] S. Ijaz, M.F. Ehsan, M.N. Ashiq, N. Karamat, T. He, Preparation of CdS@CeO₂ core/shell composite for photocatalytic reduction of CO₂ under visible-light irradiation, Appl. Surf. Sci. 390 (2016) 550–559.

[48] Z.A. Zang, H.B. Yao, Y.X. Zhou, W.T. Yao, S.H. Yu, Synthesis and magnetic properties of new [Fe₁₈S₂₅](TETAH)₁₄(TETAH = protonated triethylenetetramine) nanoribbons: An efficient precursor to Fe₇S₈ nanowires and porous Fe₂O₃ nanorods, Chem. Mater. 20 (2008) 4749–4755.

[49] M.R. Gao, W.T. Yao, H.B. Yao, S.H. Yu, Synthesis of unique ultrathin lamellar mesostructured CoSe₂-amine (Protonated) nanobelts in a binary solution, J. Am. Chem. Soc. 131 (2009) 7486–7487.

[50] J. Lv, J. Zhang, K. Dai, C. Liang, G. Zhu, Z. Wang, Z. Li, Controllable synthesis of inorganic–organic Zn₁₋ₓCdₓS-DETA solid solution nanoflowers and their enhanced

[51] Y. Oh, X. Hu, Organic molecules as mediators and catalysts for photocatalytic and electrocatalytic CO₂ reduction, Chem. Soc. Rev. 42 (2013) 2253–2261.

[52] J. Lv, J. Liu, J. Zhang, K. Dai, C. Liang, Z. Wang, G. Zhu, Construction of organic-inorganic cadmium sulfide/diethylenetriamine hybrids for efficient photocatalytic hydrogen production, J. Colloid Interf. Sci. 512 (2018) 77–85.

[53] Kai Dai, Jiali Lv, Jinfeng Zhang, Guangping Zhu, Lei Geng, Changhao Liang, Efficient visible-light-driven splitting of water into hydrogen over surface-fluorinated anatase TiO₂ nanosheets with exposed {001} facets/layered CdS-diethylenetriamine nanobelts, ACS Sustainable Chem. Eng. (2018), https://doi.org/10.1021/acssuschemeng.8b02064.

[54] K. Dai, L. Lu, C. Liang, Q. Liu, G. Zhu, Heterojunction of facet coupled g-C₃N₄/surface-fluorinated TiO₂ nanosheets for organic pollutants degradation under visible LED light irradiation, Appl. Catal. B: Environ. 156–157 (2014) 331–340.

[55] J. Jin, J. Yu, D. Guo, C. Cui, W. Ho, A hierarchical Z-scheme CdS-WO₃ photocatalyst with enhanced CO₂ reduction activity, Small 11 (2015) 5262–5271.

[56] T.J. Whittles, L.A. Burton, J.M. Skelton, A. Walsh, T.D. Veal, V.R. Dhanak, Band Alignments, Valence bands, and core levels in the Tin sulfides SnS, SnS₂, and Sn₂S₃: experiment and theory, Chem. Mater. 28 (2016) 3718–3726.

[57] M.M. Bletskan, D.I. Bletskan, Electronic structure of Sn₂S₃ compound with the mixed valency of tin, J. Optoelectron. Adv. Mater. 16 (2014) 659–664.

[58] K. Dai, L. Lu, C. Liang, G. Zhu, Q. Liu, L. Geng, J. He, A high efficient graphitic-C₃N₄/BiOI/graphene oxide ternary nanocomposite heterostructured photocatalyst with graphene oxide as electron transport buffer material, Dalton Trans. 44 (2015) 7903–7910.

[59] F. Dong, Z. Zhao, T. Xiong, Z. Ni, W. Zhang, Y. Sun, W.-K. Ho, In situ construction of g-C₃N₄/g-C₃N₄ metal-free heterojunction for enhanced visible-light photocatalysis, ACS Appl. Mater. Interfaces 5 (2013) 11392–11401.

[60] Y.R. Zheng, M.R. Gao, Q. Gao, H.H. Li, J. Xu, Z.Y. Wu, S.H. Yu, An efficient CeO₂/CoSe₂ nanobelt composite for electrochemical water oxidation, Small 11 (2015) 182–188.

[61] S. Hu, Y. Li, F. Li, Z. Fan, H. Ma, W. Li, X. Kang, Construction of g-C₃N₄/Zn₀.₁₁Sn₀.₁₂Cd₀.₈₈S₁.₁₂ hybrid heterojunction catalyst with outstanding nitrogen photofixation performance induced by sulfur vacancies, ACS Sustain. Chem. Eng. 4 (2016) 2269–2278.

[62] P. Xia, B. Zhu, B. Cheng, J. Yu, J. Xu, 2D/2D g-C₃N₄/MnO₂ nanocomposite as a direct Z-scheme photocatalyst for enhanced photocatalytic activity, ACS Sustain. Chem. Eng. 6 (2018) 965–973.

[63] J. Duan, S. Chen, M. Jaroniec, S.Z. Qiao, Porous C₃N₄ nanolayers@N-graphene films as catalyst electrodes for highly efficient hydrogen evolution, ACS Nano 9 (2015) 931–940.

[64] M. Ji, J. Di, Y. Ge, J. Xia, H. Li, 2D-2D stacking of graphene-like g-C₃N₄/Ultrathin Bi₄O₅Br₂ with matched energy band structure towards antibiotic removal, Appl. Surf. Sci. 413 (2017) 372–380.

[65] Z. Wang, J. Lv, J. Zhang, K. Dai, C. Liang, Facile synthesis of Z-scheme BiVO₄/porous graphite carbon nitride heterojunction for enhanced visible-light-driven photocatalyst, Appl. Surf. Sci. 430 (2018) 595–602.

[66] D. Das, R.K. Dutta, A novel method of synthesis of small band gap SnS nanorods and its efficient photocatalytic dye degradation, J. Colloid Interface Sci. 457 (2015) 339–344.

[67] J.F. Zhang, W.L. Yu, J.J. Liu, B.S. Liu, Illustration of high-active Ag₂CrO₄ photocatalyst from the first-principle calculation of electronic structures and carrier effective mass, Appl. Surf. Sci. 358 (2015) 457–462.

[68] J.F. Zhang, S. Wageh, A. Al-Ghamdic, J.G. Yu, New understanding on the different photocatalytic activity of wurtzite and zinc-blende CdS, Appl. Catal. B: Environ. 192 (2016) 101–107.

[69] X.C. Ma, Y. Dai, M. Guo, B.B. Huang, The role of effective mass of carrier in the photocatalytic behavior of silver halide-based Ag@AgX (X=Cl, Br, I): a theoretical study, ChemPhysChem 13 (2012) 2304–2309.

[70] S. Bai, X.J. Wang, C.Y. Hu, M.L. Xie, J. Jiang, Y.J. Xiong, Two-dimensional g-C₃N₄: an ideal platform for examining facet selectivity of metal co-catalysts in photocatalysis, Chem. Commun. 50 (2014) 6094–6097.

[71] G. Gao, Y. Jiao, E.R. Waclawik, A. Du, Single Atom (Pd/Pt) supported on graphitic carbon nitride as an efficient photocatalyst for visible-light reduction of carbon dioxide, J. Am. Chem. Soc. 138 (2016) 6292–6297.

[72] Z. Huang, X. Zeng, K. Li, S. Gao, Q. Wang, J. Lu, Z-Scheme NiTiO₃/g-C₃N₄ heterojunctions with enhanced photoelectrochemical and photocatalytic performances under visible LED light irradiation, ACS Appl. Mater. Interfaces 9 (2017) 41120–41125.

[73] Q. Liu, J. Huan, N. Hao, J. Qian, H. Mao, K. Wang, Engineering of heterojunction-mediated biointerface for photoelectrochemical aptasensing: case of direct Z-scheme CdTe-Bi₂S₃ heterojunction with improved visible-light-driven photoelectrical conversion efficiency, ACS Appl. Mater. Interfaces 9 (2017) 18369–18376.